Nanoscale
Advances

ROYAL SOCIETY
OF CHEMISTRY

PAPER

View Article Online
View Journal | View Issue

Cite this: *Nanoscale Adv.*, 2025, 7, 2309

Unraveling the roles of pressure, oxidation state, and morphology in CO_2 electroreduction to C_{2+} gaseous products over copper oxides†

Asghar Ali[ab] and Ali S. Alnaser *[abc]

Received 6th December 2024
Accepted 19th February 2025

DOI: 10.1039/d4na01019a

rsc.li/nanoscale-advances

This study provides compelling experimental evidence of the synergistic effects of reaction pressure, oxidation state, and catalyst morphology on the C_{2+} selectivity of copper (Cu) oxide catalysts in electrochemical CO_2 reduction (ECR). We employed femtosecond laser structuring and thermal treatments to synthesize Cu(0), Cu(I), Cu(II), and a mixed oxidation state catalyst Cu(*x*) with characteristic micro- and nano-morphologies. The optimal CO_2 pressure for maximizing C_{2+} productivity in aqueous bicarbonate media was established by assessing the reaction products at different imposed pressures in a custom-designed, pressurizable two-compartment cell. Among Cu(0), Cu(I), and Cu(II), thermally produced Cu(I) was the only unstructured catalyst exhibiting ethylene gas-phase selectivity. Nanostructuring enhanced the C_{2+} selectivity such that all three oxidation states could produce ethylene. More importantly, the nanostructured Cu(*x*) comprising well-dispersed Cu(0), Cu(I), and Cu(II), exhibited ethylene as well as ethane production – a characteristic associated with the synergistic effects of undercoordinated Cu states in stabilizing reaction intermediates and facilitating charge transfer to yield longer C_{2+} products. This work provides important insights into the key factors influencing C_{2+} selectivity in Cu-based catalysts, establishing the basis for an informed design to yield high-energy density products.

Introduction

Electrochemical CO_2 reduction (ECR) is a promising approach to mitigate anthropogenic CO_2 and simultaneously produce fuels and other value-added chemicals by electrocatalytically reducing CO_2. ECR is a sustainable net-zero emissions strategy for climate remediation, energy security, and long-term energy storage. Among the array of chemicals producible through ECR, some important products are carbon monoxide (CO), formate ($HCOO^-$), methane (CH_4), methanol (CH_3OH), ethylene (C_2H_4), ethane (C_2H_6), ethanol (C_2H_5OH), and propanol (C_3H_7OH). The multi-carbon (C_{2+}) products, which comprise two or more carbon (C) atoms such as ethylene, ethanol, propanol, *etc.* are attractive due to their high-energy densities, easy utilization, and industrial relevance.[1–8,9]

The surface coverage by the ECR intermediates is crucial in dictating the selectivity of a catalyst. The reaction rate and selectivity of ECR are intricately linked to the surface coverage by CO_2.[10] The local CO_2 concentration along the electrode surface affects the coverage by reaction intermediates such as $*CO_2$, *CO, and *H. Thus, the activity and selectivity of ECR are strongly influenced by CO_2 availability.[11] Among the strategies adopted to improve CO_2 availability at the electrode is the use of ionic liquids instead of water-based electrolytes.[12] Due to their high CO_2 absorption capacity, thermodynamic stability, and non-volatility, ionic liquids are employed for CO_2 capture.[13,14] Ionic liquids have garnered significant attention in ECR owing to their high ionic conductivity, ability to stabilize reaction intermediates, electrochemical stability, capacity to lower overpotentials, and structural tunability. These physicochemical attributes position ionic liquids as critical for integrated CO_2 capture and conversion.[12] However, their high cost mainly prohibits their large-scale industrial adoption. In contrast, elevating the pressure is a relatively more affordable strategy to improve CO_2 solubility in aqueous electrolytes.[15] Pressure incursions in aqueous bicarbonates can also suppress the competing hydrogen evolution reaction (HER) and thus improve ECR selectivity.[11] However, a moderate local CO_2 concentration is crucial for realizing high C_{2+} selectivity.[16] It is therefore imperative to estimate the optimum CO_2 pressure required for realize high C_{2+} selectivity on any desired catalyst in bicarbonate media.

Copper (Cu)-based catalysts are known for selectively yielding high-energy density C_{2+} products.[1,15] The C_{2+} selectivity

---

[a] *Materials Science and Engineering Program, Materials Research Center, College of Arts and Sciences, American University of Sharjah, Sharjah, UAE. E-mail: aalnaser@aus.edu*

[b] *Department of Physics, College of Arts and Sciences, American University of Sharjah, Sharjah, UAE*

[c] *Materials Research Center, American University of Sharjah, Sharjah, UAE*

† Electronic supplementary information (ESI) available. See DOI: **https://doi.org/10.1039/d4na01019a**

of Cu-based catalysts is attributed to their intermediate binding interaction with key reaction intermediates, which in turn depends on the electronic structure and oxidation state of Cu.[17,18] Cu catalysts typically exhibit Cu(0), Cu(I), and Cu(II) oxidation states.[19] Cu(0) and Cu(I) are reportedly more attractive for ECR due to their moderate binding energies towards reaction intermediates such as adsorbed CO (*CO), facilitating C–C coupling.[17,18] Recent studies also suggest that the coexistence of Cu(0) and Cu(I) centers in close vicinity is important for realizing C–C coupling.[17] Yet there are studies that suggest that Cu(I) is the actual catalytic center responsible for C–C coupling and stabilizing the intermediates,[20–23] and Cu(0) and Cu(II) might transform into Cu(I) for participating in certain catalytic reactions.[24] Nonetheless, these studies are often performed on catalysts with varying nanostructures, and the role of catalyst morphology is frequently overlooked, resulting in disparities when interpreting the observed results.

The structure and morphology of the catalysts are also key factors in determining ECR selectivity.[15] Nanomorphology promote ECR through improved selectivity.[25] This is because the coordination geometry affects the electronic structure of the catalyst, thus influencing its selectivity.[23] Smaller sized nanofeatures result in undercoordination and expose high-index facets, which promote C–C coupling by stabilizing the reaction intermediates.[26,27] In this regard, steps, nanofeatures, hierarchical structures, nanocubes, and nanograin boundaries are known to promote C_{2+} selectivity.[28,29] Uneven nanosheet structures can also lead to electron perturbation and modified electron distribution, which can affect the adsorption kinetics and module selectivity. Cubic, hexarhombic, dodecahedral, and octahedral Cu nanoparticles have been shown to significantly affect the Faradaic efficiency (FE) of both gas and liquid products.[30] Due to the undeniable importance of catalyst morphology in determining selectivity, the morphological effects should be considered in correlation with the oxidation state effects on ECR selectivity. Moreover, catalyst stability is also critical as the oxidation state and morphology may change under ECR conditions, thus influencing the product distribution.[17,18]

This study experimentally explores the complex relationship between reaction pressure, oxidation state, and catalyst morphology in influencing the C_{2+} selectivity of Cu-based electrocatalysts. Through the application of femtosecond laser surface structuring and thermal treatment procedures, we synthesize Cu(0), Cu(I), Cu(II), and mixed oxidation state Cu(x) catalysts of characteristic micro and nano-morphologies. The optimum pressure conditions for realizing high C_{2+} selectivity are investigated in a custom-designed two compartment reactor in bicarbonate media. A comprehensive analysis of the effects of Cu oxidation states in correlation with catalyst morphologies on the C_{2+} selectivity is provided. The role of undercoordinated mixed oxidation states of Cu(0), Cu(I), and Cu(II) in ethane selectivity is investigated. Lastly, the stability of the catalysts under operating conditions is evaluated. This study provides important experimental evidence of the key factors influencing the C_{2+} selectivity of Cu-based catalysts, providing valuable insights for the informed design of advanced Cu-based electrocatalysts.

Experimental

Copper substrates (1 mm thickness) were cut into 1.7 cm diameter discs. The Cu discs were subsequently ground and polished with a grinder and polisher (Forcipol 102, Metkon). These discs were subsequently cleaned with deionized water, ethanol, and acetone. For surface structuring, these samples were subjected to femtosecond laser scanning. A ytterbium-based femtosecond laser (AFSUFFL-300-2000-1030-300, Active Fiber Systems GmbH) with a central wavelength of 1030 nm, 40 fs pulse duration, and a 50 kHz repetition rate was used. A Gaussian beam was directed through a half-waveplate ($\lambda/2$) plate and a thin-film polarizer to adjust and achieve an output power of 5 W. The beam was focused onto a 50 μm spot size using an $f - \theta$ lens on a computer programmable scan head. The beam was scanned at a speed of 10 mm s^{-1}, in either a single parallel or a 5 crosshatch scan configuration. The line spacing was 20 and 70 μm for the parallel and crosshatch scans, respectively. For introducing oxides, structuring was performed in air, otherwise it was conducted in an Ar filled chamber to avoid oxidation. To further reduce samples, electrochemical reduction was conducted at -5 mA cm^{-2} for 3 minutes. Thermal treatments were carried out in a tube furnace (OTF-1200X, MTI) at 220 °C and 350 °C.

The morphology of the samples was characterized using a scanning electron microscope (VEGA-3 LMU, TESCAN). Elemental composition was determined using an energy dispersive X-ray spectroscope (EDX, INCAx-act, Oxford Instruments) fitted onto the scanning electron microscope. Further chemical insights were acquired with a confocal Raman imaging microscope (alpha300 R, WITec, Germany). A 10× objective lens was used to focus a 532 nm green laser onto the sample. Further information about the oxidation states was acquired with X-ray photoelectron spectroscopy (Nexsa G2, Thermo Scientific) using Al Kα X-rays ($h\nu = 1486.6$ eV). The resolution of the high resolution spectra was 0.1 eV and the spectra provided here are the average counts per second taken over 5 scans. XPS depth profiles were recorded after etching with Ar^+ ions using a monoatomic etcher (MAGCIS). Baseline correction, curve fitting, and area integration were performed with OriginPro 2021b (version: 9.8.5.204 (Academic)).

Electrochemical measurements were performed in a custom-designed Teflon lined two compartment stainless steel reactor with a Nafion-212 membrane separating the two compartments. Ag/AgCl (3 M) and platinum wire were used as the reference and counter electrodes, respectively. For saturation and pressure balancing, the catholyte and anolyte compartments, each containing ~100 ml of 0.1 M $NaHCO_3$, were sparged independently with pressurized CO_2 at a flow rate of ~30 sccm. The catholyte was sparged using a specially designed 3D-printed sparge head submerged in the solution. The pressure was varied in the range of 1–4.5 bar (absolute). For galvanostatic measurements, the current was maintained at -10 mA cm^{-2}, whereas potentiostatic measurements were carried out at -2 V *vs.* Ag/AgCl (3 M). An Autolab VIONIC potentiostat/galvanostat (Metrohm) was employed. Unless otherwise specified, all reported potentials are relative to Ag/AgCl (3 M), without conversion to the reversible hydrogen electrode (RHE). The gas product line from the cathode compartment was connected to an Agilent 990 micro GC for product analysis. The GC uses thermal conductivity detectors (TCD) to quantify H_2, CO, CH_4, C_2H_4, and C_2H_6. The reproducibility of the GC measurements was constantly monitored with a standard gaseous mixture. Each result reported here has been reproduced at least three times. FE was calculated using the following equation:

$$\mathrm{FE}\ (\%) = nZF/Q$$

where n is the number of moles of the product under consideration, Z is the number of electrons transferred to produce a product molecule, F is the Faraday constant (96 485 C mol^{-1}), and Q is the total charge consumed during the reaction.

Results and discussion

It is known that metallic Cu, when thermally treated in air at lower temperatures around 220 °C yields only Cu(I) oxide, whereas Cu(II) starts to form only above 320 °C.[31] Based on these findings, we produce Cu(I)- and Cu(II)-rich catalysts *via* simple furnace treatments. Fig. 1 shows flat Cu substrates, thermally treated at different temperatures to realize the desired unstructured Cu(0), Cu(I), and Cu(II) oxidation states. Fig. 1(a) present the SEM image of a ground and polished Cu surface with the corresponding EDS maps shown in Fig. 1(d and g). The elemental composition (Fig. S1†) summarized in Fig. 1(j) reveals that mechanical grinding and subsequent polishing removed most of the surface oxides from the Cu surface to form Cu(0). Since the sample is mostly metallic Cu, based on the oxidation state, we designate this sample as Cu(0). The surface after thermal treatment at 220 °C is shown in Fig. 1(b) and the corresponding elemental maps are shown in Fig. 1(e and h). The elemental composition (Fig. S2†) summarized in Fig. 1(k), depicts oxidation of the surface with thermal treatment. We designate this unstructured sample as Cu(I). The surface of polished Cu after thermal at 350 °C is shown in Fig. 1(c) with the corresponding elemental maps shown in Fig. 1(f and i). The elemental composition (Fig. S3†) outlined in Fig. 1(l), indicates strong oxidation of the Cu surface. Based on the treatment temperature and the resulting Cu : O ratio, the sample will henceforth be referred to as Cu(II).

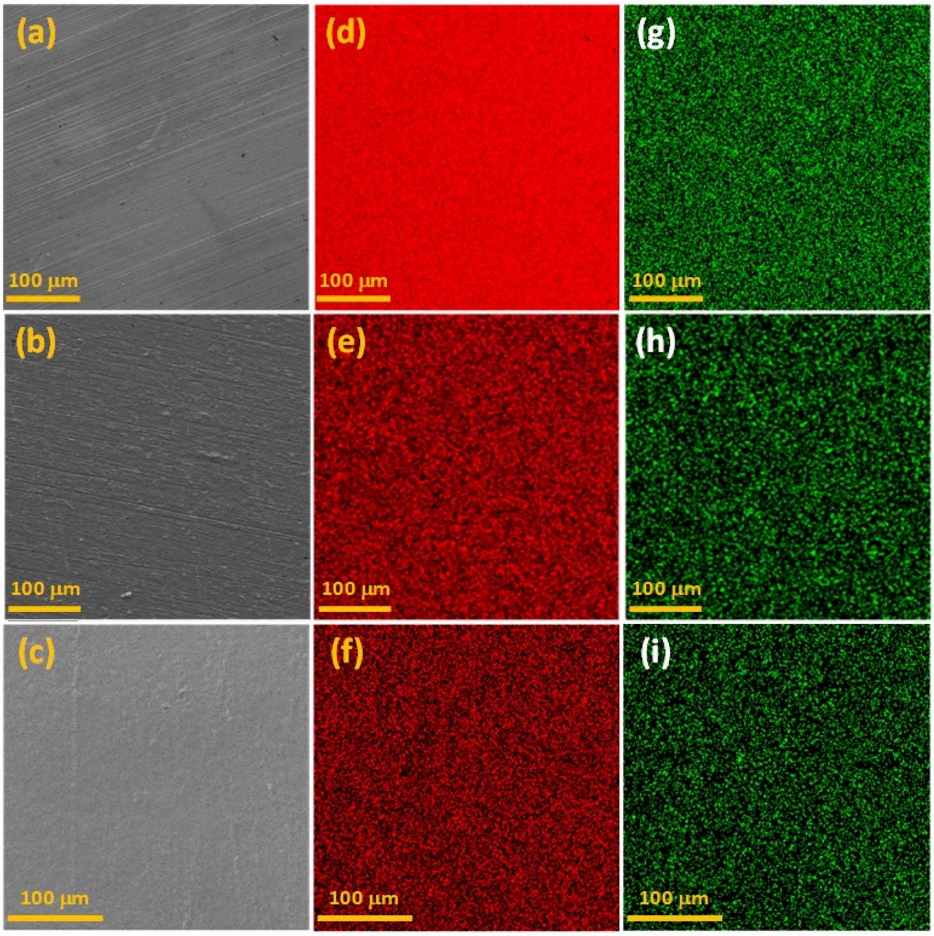

(j)

Element	Atomic %
Cu	98.55
O	1.45
Total	100.00

(k)

Element	Atomic %
Cu	64.05
O	35.95
Total	100.00

(l)

Element	Atomic %
Cu	50.06
O	49.94
Total	100.00

Fig. 1 (a–c) SEM micrographs of unstructured Cu surfaces subjected to different thermal treatments: (a) untreated, (b) treated at 220 °C, and (c) treated at 350 °C. EDS maps illustrating the distribution of (d–f) Cu and (g–i) O on the corresponding surfaces shown in (a–c). (j–l) Tables summarizing the percentage elemental composition of Cu and O along the corresponding (a–c) surfaces.

It is noteworthy that the thermal treatments affect not only the oxidation but also the surface nanomorphology. Treatment at 220 °C roughened the surface with some nanofeatures appearing on the surface due to surface reconstruction upon oxidation (Fig. S4(a)†). Similarly, treatment at 350 °C resulted in CuO nanowires along the surface (Fig. S4(b)†). These CuO nanowires are discussed in more detail in the following discussion on catalyst morphology.

Different surface morphologies were produced with femtosecond laser surface structuring and subsequent thermal treatments. Fig. 2(a) depicts a highly roughened Cu surface produced by structuring in Ar. Its elemental distribution maps are shown in Fig. 2(d and g), with the elemental composition (Fig. S5†) summarized in Fig. 2(j). The ~4.4 at% O content indicates that the microstructure is primarily composed of metallic Cu(0), and will be referred to as s-Cu(0) (here, s denotes laser-structured). Similarly, Fig. 2(b), depicts a cauliflower-shaped microstructure produced with femtosecond laser structuring in air. The corresponding elemental distribution maps are shown in Fig. 2(e and h), whereas the elemental composition (Fig. S6†) is summarized in Fig. 2(k). Due to the unknown oxidation state of this sample, we refer to it as s-Cu(x) (x denotes the unknown oxidation state). To create a highly rough Cu(II) surface, the laser structured Cu (mentioned above) was thermally treated at 350 °C in air. The corresponding morphology and elemental maps are shown in Fig. 2(c), (f) and (i), respectively. Its elemental composition (Fig. S7†) is summarized in Fig. 2(l). The thermal treatment temperature and the resulting Cu : O indicate Cu(II) oxidation. This sample will be called s-Cu(II) through the remainder of this study.

To explore the nanomorphology of the surface, further SEM analysis was performed (Fig. 3). Fig. 3(a, d) show s-Cu(0) with hierarchical surface structures, comprising Cu(0) submicron particles and nanospheres superimposed on the microstructures. Similarly, Fig. 3(b, e) show s-Cu(x), depicting cauliflower-shaped microstructures decorated with spheres of submicron and nano-sizes. Similarly, Fig. 3(c, f) shows s-Cu(II) (350 °C treated s-Cu(x)), depicting the cauliflower shaped microstructures adorned with thermally grown Cu(II) nanowires.

Dome microstructures decorated with nanofeatures were produced with femtosecond laser scanning in a crosshatch configuration (Fig. 4). Fig. 4(a and b) show Cu structured in air

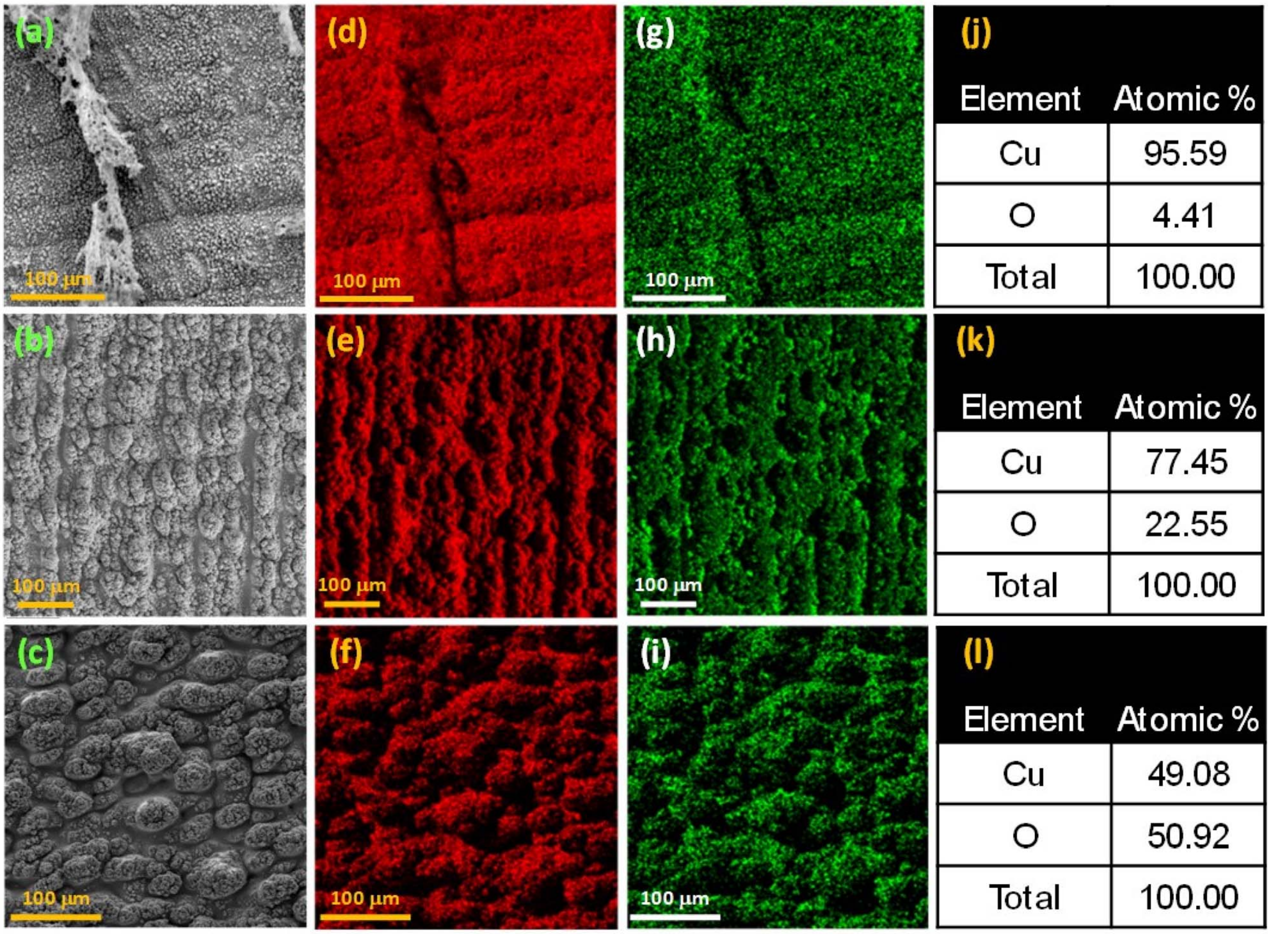

(j)

Element	Atomic %
Cu	95.59
O	4.41
Total	100.00

(k)

Element	Atomic %
Cu	77.45
O	22.55
Total	100.00

(l)

Element	Atomic %
Cu	49.08
O	50.92
Total	100.00

Fig. 2 (a–c) SEM micrographs of femtosecond laser structured Cu (with 20 μm parallel line spacing) followed by thermal treatment: (a) structured in Ar and no thermal treatment, (b) structured in air and no thermal treatment, (c) structured and thermally treated at 350 °C in air. EDS maps illustrating the distribution of (d–f) Cu and (g–i) O on the corresponding surfaces shown in (a–c). (j–l) Tables summarizing the percentage elemental composition of Cu and O along the corresponding surfaces shown in (a–c).

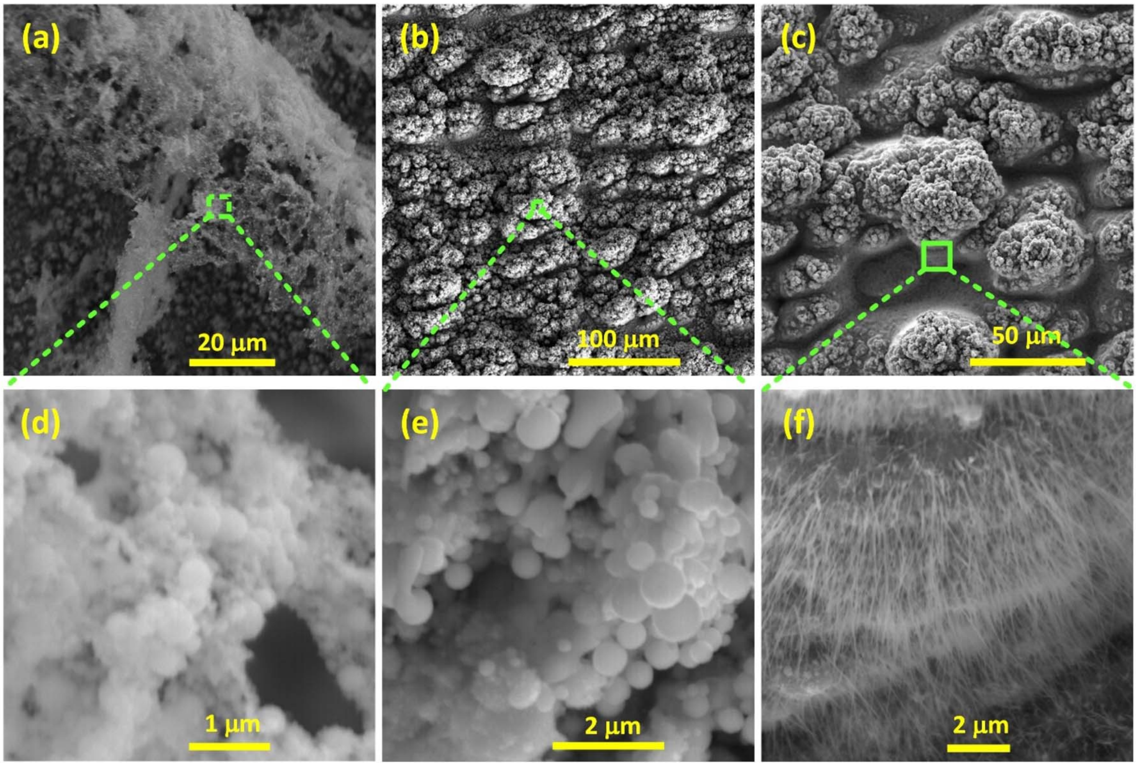

Fig. 3 (a–c) SEM micrographs of femtosecond laser-structured Cu (20 μm parallel line spacing), with (d–f) corresponding zoomed-in views. (a–d) Cu structured in Ar, showing spherical submicron and nanoparticles. (b–e) Cu structured in air, showing spherical submicron and nanoparticles. (c–f) Cu structured in air and annealed at 350 °C, depicting nanowire-decorated microfeatures.

without any subsequent thermal treatment. Hierarchical structures comprising submicron and nano-sized spheres of substoichiometric O (Fig. S8†), decorating the dome microstructures could be witnessed. Similarly, Fig. 4(c and d) represent Cu crosshatched as described above, followed by annealing at 350 °C in air. Hierarchical structures comprising Cu(II) (Fig. S9†) nanowires decorating the microdomes were observed. Due to the peculiar dome structured (ds) morphology and the O content, these samples will be referred to as ds-Cu(*x*) (where *x* represents substoichiometry) and ds-Cu(II) throughout this study.

The nanowires observed above, are actually CuO crystals, which only appear at higher temperatures (350–964 °C). CuO nanowire growth is not sustainable below 350 °C, and typically Cu_2O forms at ∼250 °C.[32,33] Upon heating, Cu first oxidizes into Cu_2O, and if the temperature is feasible (≥350 °C), only then Cu_2O further oxidizes into CuO.[32–36] This is why we only observed Cu_2O nanospheres while treating Cu(0) at 220 °C. The nanowire growth is governed by the diffusion of Cu from the underlying substrate and O from the atmosphere. Upon heating, Cu atoms diffuse to the CuO/Cu_2O interface and are exchanged between the equilibrating CuO and Cu_2O phases. The Cu atoms continue hopping between the two phases until they encounter O diffusing from the atmosphere, eventually forming stable CuO; this way the nanowire keeps on growing. CuO remains stable in the O rich region above the interface, whereas Cu_2O is more stable in the relatively lower O content region below the interface.[33]

The surface chemistry was further elucidated through Raman shift analysis. Fig. 5 compares the Raman shift spectra of Cu-derived samples processed in air, *i.e.*, Cu(I), obtained by treating Cu at 220 °C; Cu(II), obtained by treating Cu at 350 °C; and s-Cu(*x*), the laser-structured Cu. The broad hump around 520 cm^{-1} is the only band with T_{2g} symmetry and is associated with the presence of Cu_2O in the Cu(I) sample. The broad hump indicates structural disorder in Cu_2O, leading to the emergence of additional peaks that are typically absent in well-ordered Cu_2O. In fact, Cu_2O is known to reveal Raman forbidden bands and that is why several other bands associated with Cu_2O were identified.[37] Among the other peaks associated with Cu_2O are those at 145 and 214 cm^{-1}.[38] The peak around 284 cm^{-1} appears as a convoluted peak with several subpeaks and may be attributed either to the second order overtone of Cu_2O or to CuO; however, the peak at around 332 cm^{-1} suggests that the 288 cm^{-1} peak is probably due to CuO.[39] The broad convoluted band around 625 cm^{-1} is even more interesting. There are instances in the literature suggesting that this band is due to Cu_2O,[40,41] whereas others attribute it to CuO.[39,42,43] Due to the considerable number of peaks detected for Cu_2O, we can confidently say that the Cu(I) sample is mainly composed of Cu_2O, but there is a fraction of CuO also present in this sample.

The Cu(II) sample (Fig. 5) is relatively straightforward and depicts all the peaks representative of CuO around 271, 321, and 600 cm^{-1}. The 271 and 321 cm^{-1} bands exhibit an almost constant shift (∼12 cm^{-1}) relative to their corresponding peaks detected in Cu(I); however, the 600 cm^{-1} band is shifted by 25 cm^{-1} from the

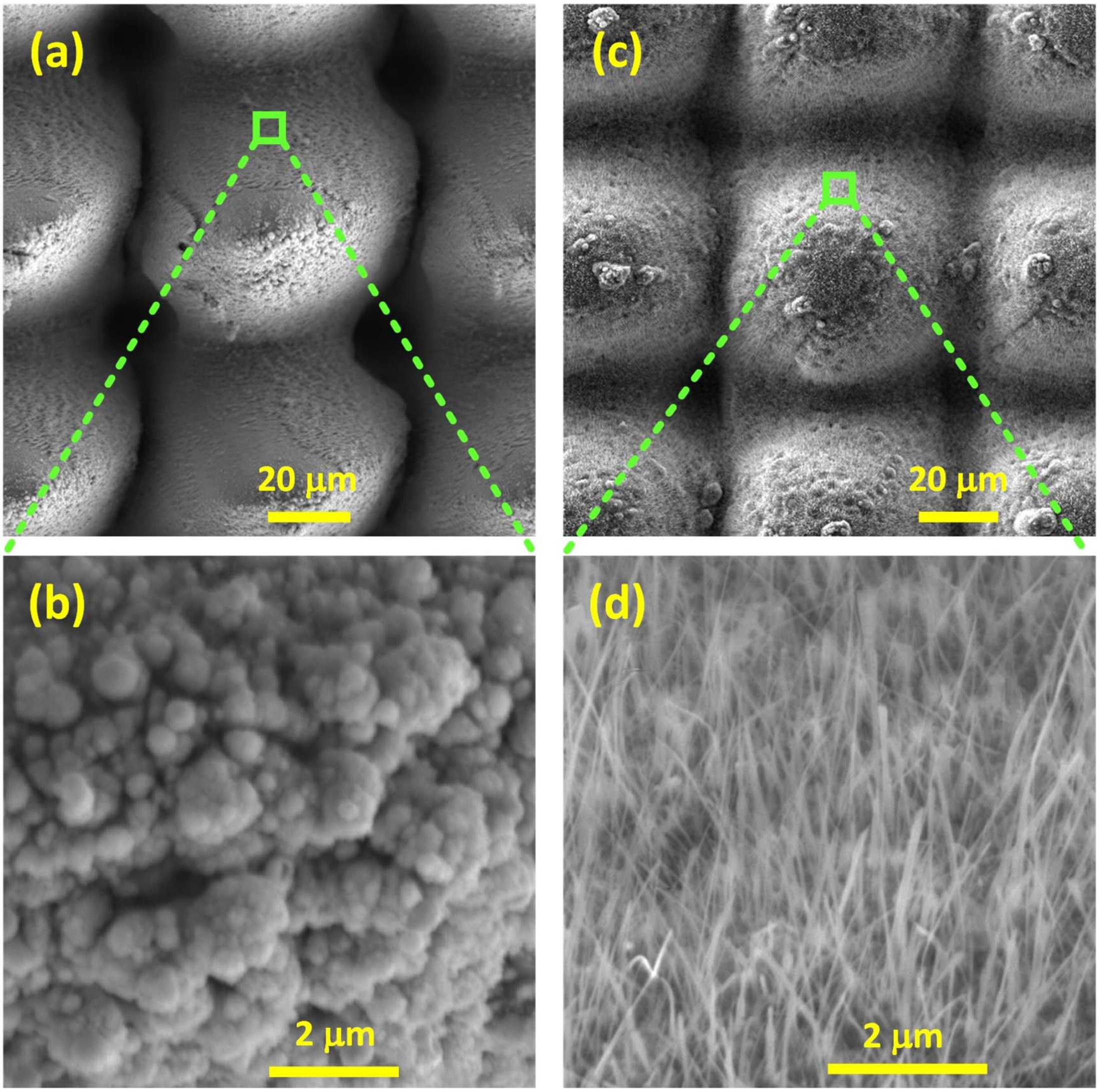

Fig. 4 SEM micrographs of femtosecond laser structured Cu (70 μm crosshatch line spacing) with (a and b) no thermal treatment depicting submicron and nanospheres decorating microdomes, and (c and d) thermally treated at 350 °C in air, showing nanowires decorating the microdomes.

625 cm^{-1} peak in Cu(I), implying that this band is more sensitive towards changes in the local chemical environment.

The s-Cu(x) (Fig. 5) sample shows the two representative bands of CuO at exactly the same position as those for Cu(I), *i.e.*, at 284 and 332 cm^{-1}. However, the band at 625 cm^{-1} in Cu(I) shifted to 613 cm^{-1} in s-Cu(x). As discussed above, this band is more sensitive to changes in the local chemical environment, showing that this sample is chemically different from both Cu(I) and Cu(II). In fact, this Raman band has been observed to shift in the 601–624 cm^{-1} range with adsorbed O.[40,44-46] As shown later in this work, s-Cu(x) is an important ECR catalyst and needs more thorough investigation. Further insights into its oxidation state and adsorbed O were acquired using XPS analysis.

Fig. 6 presents high-resolution XPS analysis of O 1s (Fig. 6(a)), Cu 2p and its depth profile (Fig. 6(b)), Cu 2p$_{3/2}$ (Fig. 6(c)), and Cu LMM Auger (Fig. 6(d)) spectra of the unused laser structured s-Cu(x). The O 1s spectrum (Fig. 6(a)) was resolved into 5 peaks at 529.7, 530.8, 531.5, 532.3, and 533.2 eV corresponding to CuO,[47-49] Cu_2O,[50] $Cu(OH)_2$,[49,51,52] C–O/COH,[47,52] and adsorbed water/O_2.,[52,53] respectively. Cu(II), existing as CuO and $Cu(OH)_2$, is apparently more abundant than Cu(I) existing as Cu_2O. Besides Cu(I), and Cu(II), the top surface also contains C impurities (organic contaminants) as well as adsorbed water and O_2. Previously, we have shown that the Raman band shift in the 600–625 cm^{-1} range may be due to this adsorbed O. To further investigate the Cu(0), Cu(I), and Cu(II) states, we explore the Cu 2p spectrum and its depth profile as the surface is etched under vacuum (Fig. 6(b)). The Cu 2p$_{1/2}$ main peak and its satellite features, along with the Cu 2p$_{3/2}$ main peak and corresponding satellites, are observed within the binding energy range of 950–967 eV and 929–947 eV, respectively.[54,55] Upon etching, a shift in peak position towards lower binding energies was witnessed, accompanied by a reduction in the satellites and

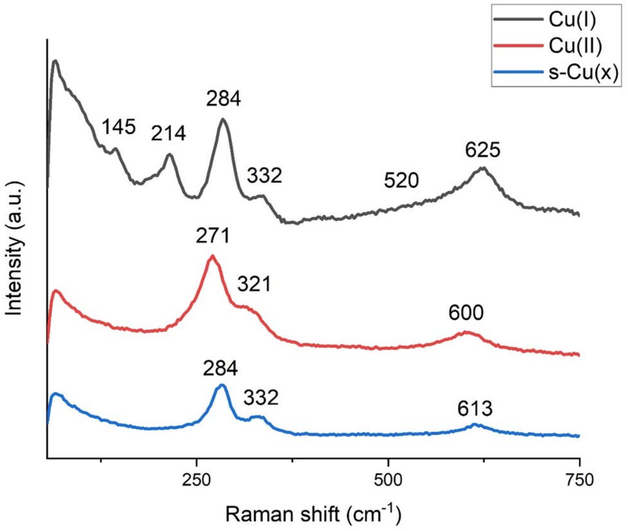

Fig. 5 Raman shift analysis of samples predominantly composed of Cu_2O, as Cu(I), CuO, as Cu(II), and laser structured Cu with mixed oxidation states, s-Cu(*x*).

sharpening of the main Cu $2p_{1/2}$ and Cu $2p_{3/2}$ peaks. A continuous decrease in Cu(II) content, likely accompanied by a reduction in O content, is suggested as we move deeper beneath the top surface (Fig. 6(b)).

Although, the Cu $2p_{3/2}$ peak hardly distinguishes Cu(0) from Cu(I), it can be used to easily quantify Cu(II) relative to Cu(0) and Cu(I) together. The strong shake-up peaks appearing at 944.1 and 941.7 eV in Fig. 6(c) indicate a considerable Cu(II) content in the unused s-Cu(*x*). Here, an indicator of the fitting accuracy is the ratio of the areas under the curve of Cu $2p_{3/2}$ and its satellites, which should be 1.89 for Cu(II). Our fitting yields the same ratio, thus confirming the reliability of the fitting for quantifying Cu(II) relative to Cu(0) and Cu(I) combined. Cu(II) constitutes ∼81.5%, whereas Cu(0) and Cu(I) together constitute ∼18.5% of the total composition. To distinguish the Cu(0) and Cu(I) components, we analyze the Cu LMM spectrum given in Fig. 6(d). The Cu LMM analysis to quantify Cu(0) and Cu(I) is especially useful when the Cu(II) content is low. This is because the relatively broad Cu(II) peaks can overshadow the Cu(0) and Cu(I) peaks, as shown in Fig. 6(d). Furthermore, Cu(0) comprises almost seven Cu LMM peaks, whereas, Cu_2O is

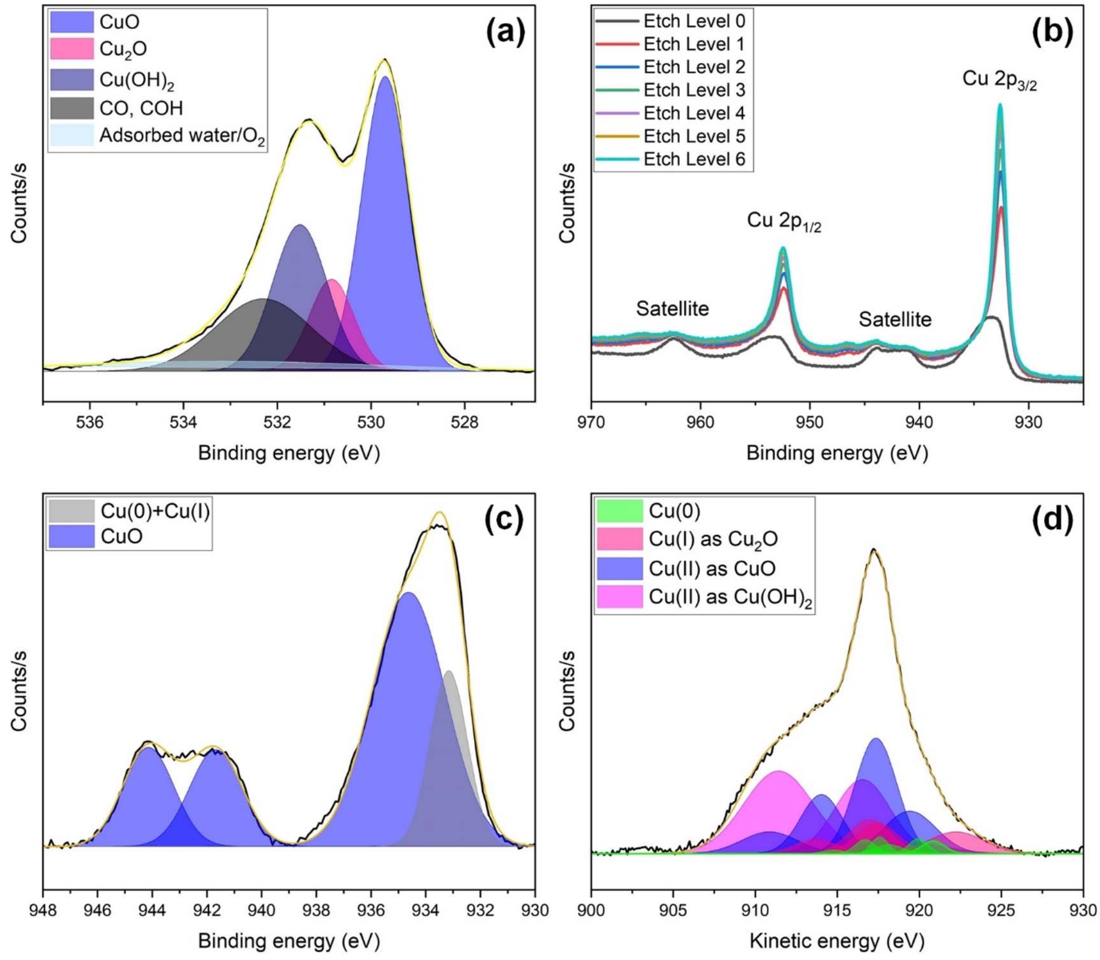

Fig. 6 High resolution XPS spectra of s-Cu(*x*) prior to ECR studies, showing (a) O 1s, (b) Cu 2p along with a depth profile, (c) Cu $2p_{3/2}$, and (d) Cu LMM Auger spectral analysis.

represented by four such peaks. Also, when the relative content of Cu(0) and/or Cu(I) is considerably lower than that of Cu(II), it becomes more challenging to precisely quantify Cu(0) and Cu(I) due to peak overlap with Cu(II).[56] The over 80% Cu(II) determined above is quite large, and although we tried, the exact quantification of Cu(I) relative to Cu(0) remains challenging based on the Cu LMM spectrum. After peak deconvolution, the characteristic peaks of Cu(0) were located at 920.84, 919.94, 918.14, 917.59, 916.7, 914.76, and 911.44 eV. Those of Cu(I) were identified at 922.24, 917.45, 916.98, and 913.69. Cu(II) in the form of CuO was identified from peaks at 919.42, 917.36, 914.04, and 910.87 eV, whereas Cu(II) as $Cu(OH)_2$ was signified by peaks at 919.61, 916.54, and 911.43 eV. The relative content of Cu(0), Cu(I), and Cu(II) confirmed from Cu LMM analysis was 5.3%, 16.4%, and 78.3%, respectively. Since the Cu(II) content calculated from the Cu LMM spectrum (*i.e.*, 78.3%) closely aligns with that from Cu $2p_{3/2}$ (*i.e.*, 81.5%), the estimated composition of Cu(0) and Cu(I) in the sample is approximately 4% and 16%, respectively. The above discussion leads us to the conclusion that the pre-ECR s-Cu(*x*) comprises mixed oxidation states, with 80% Cu(II), 16% Cu(I), and 4% Cu(0).

To quantify surface changes in oxidation state due to electrochemical CO_2 reduction, post-ECR XPS analysis of s-Cu(*x*) was also performed. Fig. 7 presents the Cu $2p_{3/2}$ (Fig. 7(a)) and Cu LMM (Fig. 7(b)) spectra of the s-Cu(*x*) sample acquired after 6 hours of chronoamperometry in $NaHCO_3$ at −2 V *vs.* Ag/AgCl (3 M), corresponding to *ca.* -10 mA cm^{-2}. Compared to the pre-ECR composition, the Cu $2p_{3/2}$ spectrum of the post-ECR sample reveals a significant reduction in the Cu(II) content (934.6 eV) relative to the Cu(0) + Cu(I) content (932.4 eV). The Cu(II) content drops to ~34%, whereas Cu(0) + Cu(I) increase to ~66%. Further insights into the relative composition were provided by the Cu LMM analysis (Fig. 7(b)). The peaks signifying Cu(0) were identified at 921.11, 919.68, 918.65, 917.77, 916.7, 913.8, and 910.48 eV. The characteristic peaks of Cu(I) were located at 922.1, 917.45, 916.45, and 913.36 eV. Similarly, Cu(II) in the form of CuO was observed at 919.4, 917.57, 913.91, and 910.87 eV. Likewise, Cu(II) as $Cu(OH)_2$ was identified by peaks at 919.8, 916.46, and 911.4 eV. Based on Cu LMM analysis, the post-ECR composition is *ca.* 32% Cu(0), 35% Cu(I), and 33% Cu(II). The findings show that during ECR, s-Cu(*x*) undergoes reduction from Cu(II) to Cu(I) and Cu(0) states. Such changes in the oxidation state during ECR, which can influence selectivity, have been witnessed in previous studies as well.[57–59]

Fig. 8(a) depicts the effects of pressure incursions on the FE for gaseous products for hierarchically structured s-Cu(*x*) (Fig. 3(b, e)). Increasing the pressure to 4.5 bars triggers suppression of the HER (FE 22%) and promotion of C_{2+} gaseous products (FE 31%). Compared to the FEs at 1 bar, the combined FE of C_2H_4 and C_2H_6 witnessed an almost 200% increase at 4.5 bar. Meanwhile H_2 experienced an ~56% decrease in FE. Almost 50% of the total FE can be associated with the liquid ECR products (assuming negligible losses). We previously quantified several of these liquid products and established that the FE of C_{2+} liquids such as ethanol and propanol is related to that of ethylene and ethane in the gaseous stream. Especially, the FE of propanol was observed to significantly increase with increasing ethane content.[60] Thus, a total FE of ~80% can be realized for all the ECR products. If ethane, ethanol, and propanol were the only chemicals produced, then the H_2 liberated, which accounts for about 20% of the total FE, would be sufficient to meet the H requirements of these products. Therefore, the 4.5 bar pressure may be considered optimal to effectively suppress HER, provided sufficient C_{2+} selectivity is observed. A further increase in pressure increases the CO yield. Based on the activity and selectivity of other catalysts, other pressure conditions might be necessary to achieve similar C_{2+} FEs.

Fig. 8(b) demonstrates the FEs of several catalysts including unstructured Cu(0), Cu(I), and Cu(II) as well as femtosecond laser structured s-Cu(0), s-Cu(*x*), and s-Cu(II) catalysts measured at 4.5 bar. As evident from Fig. 8(b), the unstructured Cu(0) mostly produces H_2 along with some CO and methane. Laser structuring enhances the C_{2+} selectivity of s-Cu(0), leading to the production of ethylene instead of methane, which is completely suppressed after structuring. In contrast to Cu(0),

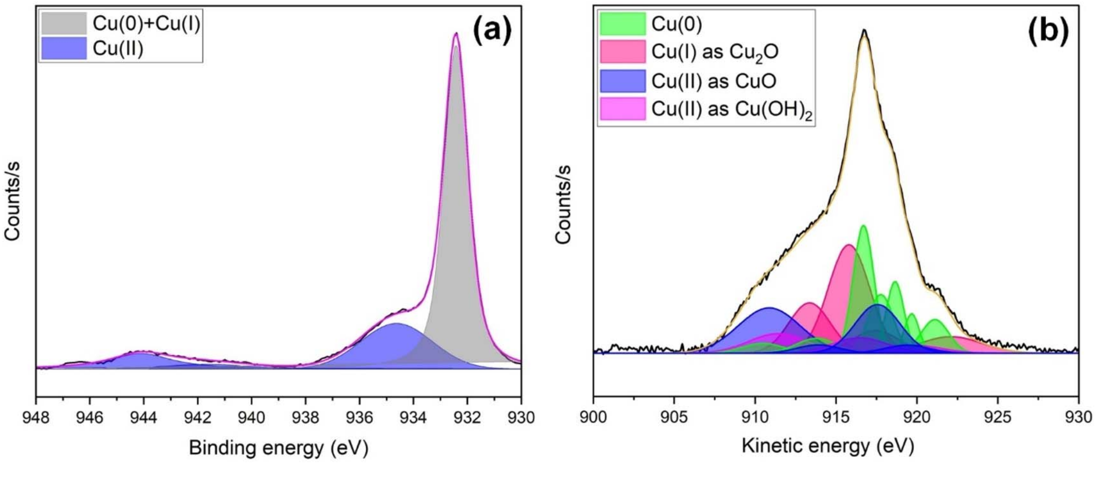

Fig. 7 High-resolution XPS spectra of s-Cu(*x*) obtained after electrochemical CO_2 reduction, presenting (a) Cu $2p_{3/2}$ and (b) Cu LMM Auger spectral analysis.

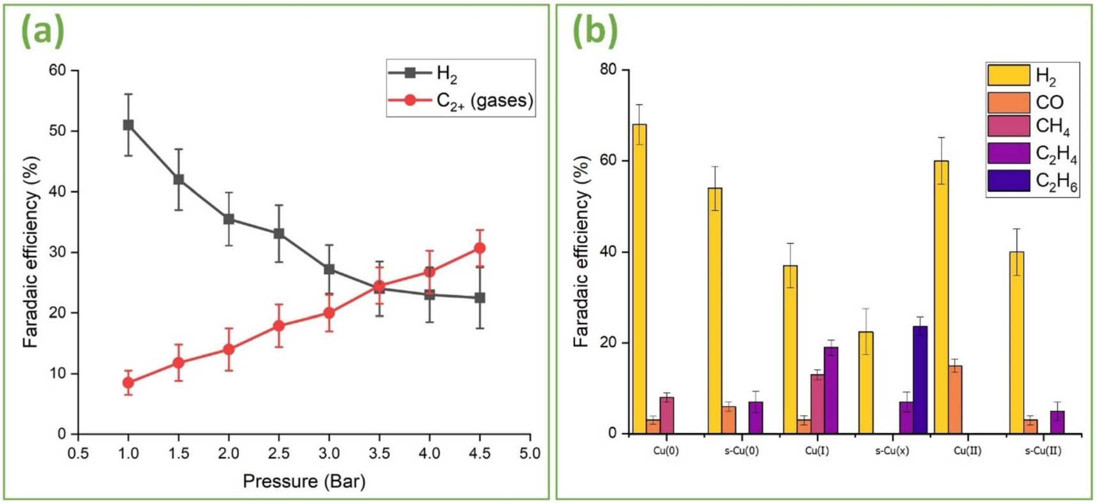

Fig. 8 (a) Faradaic efficiency of s-Cu(x) for H_2 and C_{2+} gases as a function of vessel pressure. (b) Faradaic efficiency of all gaseous products observed for unstructured and hierarchically structured Cu(0), Cu(x), and Cu(II) electrodes, respectively.

unstructured Cu(I) produces significant amounts of both methane and ethylene as well as some traces of CO. Also, the HER is relatively suppressed compared to both Cu(0) and s-Cu(0). This emphasizes the role of oxidation state in influencing the selectivity of the Cu-based catalyst. Upon femtosecond laser structuring of Cu(0) in air, we get s-Cu(x) with the highest C_{2+} selectivity, also yielding ethane along with ethylene, whereas methane is totally suppressed. Furthermore, the HER is also significantly suppressed on s-Cu(x). In contrast to unstructured Cu(I), Cu(II) can only produce CO besides H_2. Changes in the oxidation state and atomic coordination are the most probable causes for this shift in selectivity. To analyze if structuring can improve the performance of Cu(II) oxide, s-Cu(II) was analyzed and was found to produce some ethylene along with H_2 and CO. The ethylene production on s-Cu(II) (decorated with a thick forest of CuO nanowires on top of the laser-induced nanostructures) (Fig. 4(c and d)), compared to unstructured Cu(II) (with less dense nanowires and no laser structuring) (Fig. S4(b)†) underscores the significance of nanostructuring that exposes high-index facets and/or undercoordinated sites for prolonged adsorption of the intermediates. This finding aligns well with studies demonstrating that high-index facets on Cu surfaces facilitate the formation of multi-carbon products during ECR.[27]

Some researchers declare C_{2+} selectivity exclusively to Cu(I), often overlooking the role of Cu(II) altogether.[17,18,20–23] Compared to Cu(0) and Cu(II), Cu(I) boasts intermediate adsorption strength for reaction intermediates while also facilitating delocalized d-band electrons, which likely explains this conclusion. However, the results reported here, provide convincing experimental evidence that low coordinated and well-dispersed mixed oxidation states involving Cu(0), Cu(I), and Cu(II) are important for realizing C_{2+} products. The production of ethane with total suppression of methane on s-Cu(x) is an indication of the synergetic effects of low coordinated Cu(0), Cu(I), and Cu(II) in promoting C_{2+} selectivity. We believe that the low coordinated Cu(I) and/or Cu(II) provide the necessary adsorption strength to stabilize the intermediates, allowing them to remain adsorbed long enough for charge transfer to take place. However, the charge transfer is favorably facilitated by the relatively more electron rich d-band Cu(0) and Cu(I). Similarly, the relatively lower and moderate corresponding adsorption strengths of Cu(0) and Cu(I), which we believe are uniformly distributed along Cu(II), promote hopping so that longer chains *via* C–C coupling could be realized. The Raman analysis discussed above (Fig. 5), also indicates the uniform distribution of Cu(I) within the Cu(II) matrix. We observed strained broad peaks of Cu(II) that were red shifted, with no single strong peak of Cu(I) in s-Cu(x). Lower coordination and such mixed oxide distributions are typical of femtosecond lasers, which deliver very high-power pulses with time durations on the order of femtoseconds.[60–67]

The above deductions regarding the optimized adsorption strength, intermediates' mobility, and charge transfer kinetics are in line with previous claims of efficient intermediate coupling observed on composite heterostructure catalysts. Such heterostructure catalysts may favorably adsorb specific intermediates due to the distinct chemical nature of the available active sites. The heterojunctions ensure close proximity of the active sites, thus reducing energy barriers for the coupling of intermediates to realize larger molecules. The heterostructures may also promote charge transfer kinetics because of variations in charge distribution along the heterojunction interface. Such spatial and electronic integration may suppress the competing HER by facilitating coupling at the interface.[68]

To further unveil the effects of oxidation and surface structuring on C–C coupling, the dome-structured ds-Cu(x) and ds-Cu(II) (Fig. 4) catalysts were analyzed (Fig. 9). Fig. 9(a) provides FE *vs.* time plots for ds-Cu(x). Similar to the above-discussed s-Cu(x), ds-Cu(x) can also effectively suppress methane and yield C_{2+} products including ethane, although with lower FEs compared to s-Cu(x). Similarly, the HER is also less suppressed

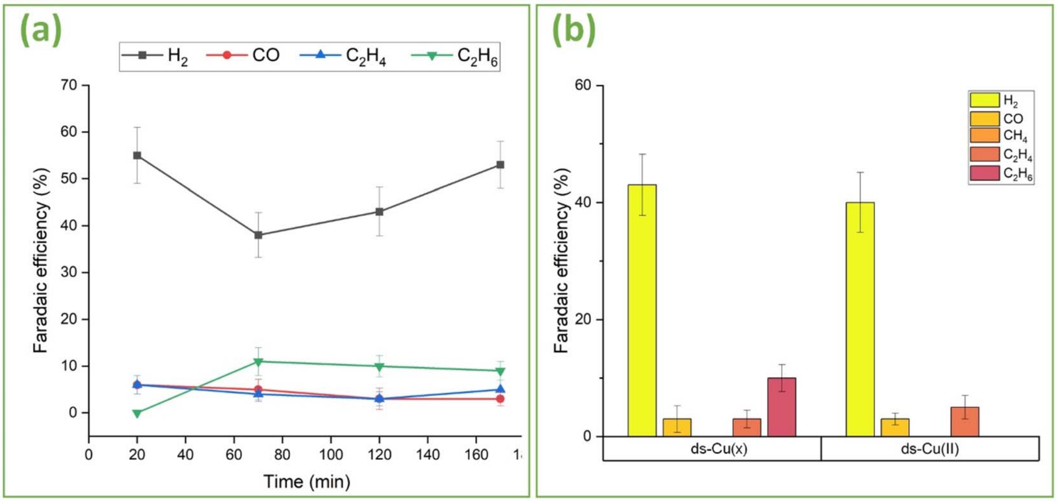

Fig. 9 (a) Faradaic efficiency of ds-Cu(x) for gaseous products as a function of time. (b) Comparison of Faradaic efficiency of ds-Cu(x) and ds-Cu(II) for gas products at 4 bar pressure.

compared to s-Cu(x). Furthermore, the FEs of most of the products including H_2, are not constant but rather change with time. The dome structured Cu(x) was produced using a set of different laser parameters compared to s-Cu(x), resulting in different morphology and chemistry compared to s-Cu(x). It is less nanorough (Fig. 3(b) *vs.* Fig. 4(a)) than s-Cu(x), which may suggest higher atomic coordination. Similarly, it is apparently more oxidized (Fig. S8† *vs.* Fig. 2(k)) than s-Cu(x), hinting at a larger proportion of Cu(II) (>81%) and a lower content of Cu(0) + Cu(I) (<19%) than on s-Cu(x). From the preceding discussion, we have discovered that mixed and well-dispersed oxides help boost the C_{2+} selectivity. With lower Cu(0) and Cu(I) content, the likelihood of intermediate adsorption (on Cu(I)) and efficient electron transfer (by both Cu(0) and Cu(I)) is reduced compared to s-Cu(x) and thus C_{2+} products are less likely on ds-Cu(x) than on s-Cu(x). For these reasons we observe relatively lower C_{2+} selectivity on ds-Cu(x). Since methane, which has the highest H : C ratio, was effectively suppressed, and other C_{2+} hydrocarbons such as ethane, which also have high H : C ratios, could not be produced efficiently, the HER consequently dominates. It is for these reasons that the FE of HER is quite high on ds-Cu(x). Furthermore, the change in selectivity with time is attributed to *in situ* changes in the oxidation state observed in this study, along with local environmental changes and surface reconstruction during ECR, as reported by others.[69–71] The observed nonproportional changes in FE over time between the reported C_{2+} gas products and H_2 are not necessarily correlated, as liquid products such as formate, methanol, ethanol, and propanol were not explored in this study.

Fig. 9(b) provides FE comparison data of ds-Cu(x) and ds-Cu(II) after two hours of operation at -10 mA cm^{-2}. Although both successfully suppress methane, ds-Cu(II) is incapable of producing ethane. Their nano-morphologies (Fig. 4(a) *vs.* (b)) reveal that although ds-Cu(II) has a very dense forest of CuO nanowires covering it, ds-Cu(x) is more selective towards longer C_{2+} products. It can be inferred that mixed oxides, even though less nanostructured, exhibit greater selectivity towards C_{2+} products than highly nanostructured Cu(II).

Conclusion

This study demonstrates the synergistic influence of reaction pressure, oxidation state, and catalyst morphology on C_{2+} selectivity of Cu-based electrocatalysts for electrochemical CO_2 reduction (ECR). Using femtosecond laser structuring and thermal treatments, we synthesized Cu(0), Cu(I), Cu(II), and mixed oxidation state Cu(x) catalysts exhibiting unique micro- and nano-morphologies. Thermally produced Cu(I) was confirmed as the only oxidation state among Cu(0), Cu(I), and Cu(II), capable of yielding ethylene without structuring. However, nanostructuring enabled all the three oxidation states to yield C_{2+} products. Notably, nanostructured Cu(x) (*i.e.*, the mixed oxidation state catalyst) was found to produce ethylene as well as ethane with a combined Faradaic efficiency (FE) of 31% at 4.5 bar, while completely suppressing methane production. The enhanced C_{2+} selectivity of structured Cu(x) was attributed to the cooperative interaction of the well-dispersed and under-coordinated Cu(0), Cu(I), and Cu(II) in promoting C–C coupling. Among the mixed states, Cu(I) and Cu(II) provide the necessary adsorption strength to stabilize the reaction intermediates, allowing them to remain adsorbed long enough to facilitate coupling. Due to the more filled d-orbitals, charge transfer is more favored on Cu(0) and Cu(I) relative to Cu(II) with less filled d-orbital. Similarly, the relatively lower adsorption strength of Cu(0) and Cu(I) helps in the hopping of reaction intermediates so that longer chains *via* C–C coupling could be realized. Lastly, elevating CO_2 pressures up to 4.5 bar was also witnessed to improve C_{2+} yield, with combined gaseous C_{2+} FEs increasing by ~200% relative to 1 bar, while suppressing H_2 FE by ~56%. The findings presented here enrich our understanding of the key factors influencing multicarbon product selectivity and provide important insights for the design of advanced Cu-based electrocatalysts for selective CO_2 reduction.

Data availability

For access to the datasets used and/or analyzed in this study, please contact the corresponding author.

Author contributions

Asghar Ali: conceptualization, writing the original draft, methodology, investigation, formal analysis, data curation. Ali. S. Alnaser: conceptualization, review & editing, supervision, project administration, funding acquisition.

Conflicts of interest

The authors have no conflict to declare.

Acknowledgements

This study was funded by the American University of Sharjah under grant no. FRG23-C-S55. We are thankful to Professor Hussain Alawadhi of the University of Sharjah for the XPS measurements.

References

1 A. D. Handoko, K. W. Chan and B. S. Yeo, CH3 Mediated Pathway for the Electroreduction of CO2 to Ethane and Ethanol on Thick Oxide-Derived Copper Catalysts at Low Overpotentials, *ACS Energy Lett.*, 2017, **2**(9), 2103–2109, DOI: **10.1021/ACSENERGYLETT.7B00514**.

2 H. Mistry, A. Varela, C. Bonifacio, I. Zegkinoglou, I. Sinev, Y. W. Choi, K. Kisslinger, E. Stach, J. Yang, P. Strasser and B. Cuenya, Highly selective plasma-activated copper catalysts for carbon dioxide reduction to ethylene, *Nat. Commun.*, 2016, **7**(1), 12123, DOI: **10.1038/ncomms12123**.

3 A. Eilert, *et al.*, Subsurface Oxygen in Oxide-Derived Copper Electrocatalysts for Carbon Dioxide Reduction, *J. Phys. Chem. Lett.*, 2017, **8**(1), 285–290, DOI: **10.1021/ACS.JPCLETT.6B02273**.

4 D. Ren, Y. Deng, A. D. Handoko, C. S. Chen, S. Malkhandi and B. S. Yeo, Selective Electrochemical Reduction of Carbon Dioxide to Ethylene and Ethanol on Copper(I) oxide catalysts, *ACS Catal.*, 2015, **5**(5), 2814–2821, DOI: **10.1021/CS502128Q**.

5 L. Xu, *et al.*, Identifying the optimal oxidation state of Cu for electrocatalytic reduction of CO_2 to C_{2+} products, *Green Chem.*, 2023, **25**(4), 1326–1331, DOI: **10.1039/D2GC04368H**.

6 J. J. Velasco-Vélez, *et al.*, The Role of the Copper Oxidation State in the Electrocatalytic Reduction of CO 2 into Valuable Hydrocarbons, *ACS Sustain. Chem. Eng.*, 2019, **7**(1), 1485–1492, DOI: **10.1021/ACSSUSCHEMENG.8B05106**.

7 A. M. Asiri, *et al.*, Revisiting the Impact of Morphology and Oxidation State of Cu on CO2Reduction Using Electrochemical Flow Cell, *J. Phys. Chem. Lett.*, 2022, **13**(1), 345–351, DOI: **10.1021/ACS.JPCLETT.1C03957**.

8 W. Luo, *et al.*, Selective and Stable Electroreduction of CO2 to CO at the Copper/Indium Interface, *ACS Catal.*, 2018, **8**(7), 6571–6581, DOI: **10.1021/ACSCATAL.7B04457**.

9 A. Ali, M. Qasim, S. Sakhi, G. Maduraiveeran and A. S. Alnaser, Electrochemical CO_2 reduction: Advances, insights, challenges, and future directions, *Mater. Today Sustain.*, 2025, **30**, 101089, DOI: **10.1016/j.mtsust.2025.101089**.

10 C. Chen, L. Huang, Y. Jiang, Y. Zheng and S. Z. Qiao, Modulating local environment for electrocatalytic CO2 reduction to alcohol, *Nano Energy*, 2024, **126**, 109656, DOI: **10.1016/J.NANOEN.2024.109656**.

11 D. Deciccio, S. T. Ahn, S. Sen, F. Schunk, G. T. R. Palmore and C. Rose-Petruck, Electrochemical reduction of CO2 with clathrate hydrate electrolytes and copper foam electrodes, *Electrochem. Commun.*, 2015, **52**, 13–16, DOI: **10.1016/J.ELECOM.2015.01.006**.

12 X. An, *et al.*, Application of ionic liquids in CO2 capture and electrochemical reduction: A review, *Carbon Resour. Convers.*, 2023, **6**(2), 85–97, DOI: **10.1016/J.CRCON.2023.02.003**.

13 Y. Zhao, X. Wang, Z. Li, H. Wang, Y. Zhao and J. Qiu, Understanding the Positive Role of Ionic Liquids in CO2 Capture by Poly(ethylenimine), *J. Phys. Chem. B*, 2024, **128**(4), 1079–1090, DOI: **10.1021/ACS.JPCB.3C06510**.

14 H. Zhao, T. Zhang, S. Chen and G. Zhao, Hierarchical Fibrous Metal-Organic Framework/Ionic Liquid Membranes for Efficient CO2/N2 Separation, *Nano Lett.*, 2025, DOI: **10.1021/ACS.NANOLETT.4C05232**.

15 A. Ali, M. Qasim, S. Sakhi, G. Maduraiveeran and A. S. Alnaser, Electrochemical CO2 Reduction: Advances, Insights, Challenges, and Future Directions, *Mater. Today Sustain.*, 2025, 101089, DOI: **10.1016/J.MTSUST.2025.101089**.

16 Y. Hua, J. Wang, T. Min and Z. Gao, Electrochemical CO_2 conversion towards syngas: Recent catalysts and improving strategies for ratio-tunable syngas, *J. Power Sources*, 2022, **535**, 231453, DOI: **10.1016/J.JPOWSOUR.2022.231453**.

17 S. Tafazoli, M. Yusufoğlu, T. Balkan and S. Kaya, In-situ surface enhanced Raman spectroscopy investigations on surface transformations of oxide derived copper electrodes during CO2RR, *J. Catal.*, 2023, **423**, 118–128, DOI: **10.1016/J.JCAT.2023.04.021**.

18 S. Y. Ahn, J. H. Han and H. S. Roh, Boosting the active sites of Cu/Ce0.8Zr0.2O2 catalysts through tailored precipitation method, *Chem. Eng. J.*, 2024, **499**, 155890, DOI: **10.1016/J.CEJ.2024.155890**.

19 R. Monjezi, *et al.*, Mechanistic insights into methane total oxidation over Cu/Hydroxyapatite catalyst synthesized with β-Cyclodextrin assistance, *Chem. Eng. J.*, 2024, **489**, 151324, DOI: **10.1016/J.CEJ.2024.151324**.

20 R. Bu, L. Zhang, L. L. Gao, W. J. Sun, S. L. Yang and E. Q. Gao, Copper(I)-modified covalent organic framework for CO2 insertion to terminal alkynes, *Mol. Catal.*, 2021, **499**, 111319, DOI: **10.1016/J.MCAT.2020.111319**.

21 D. E. Stephens and O. V. Larionov, Recent advances in the C–H-functionalization of the distal positions in pyridines and

quinolines, *Tetrahedron*, 2015, **71**(46), 8683–8716, DOI: **10.1016/J.TET.2015.08.034**.

22 Y. Liu, H. Liu, C. Wang, Y. Wang, J. Lu and H. Wang, Reconstructed Cu/Cu2O(I) catalyst for selective electroreduction of CO2 to C2+ products, *Electrochem. Commun.*, 2023, **150**, 107474, DOI: **10.1016/J.ELECOM.2023.107474**.

23 Z. Li, *et al.*, Boron-modified CuO as catalyst for electroreduction of CO2 towards C2+ products, *Appl. Surf. Sci.*, 2024, **647**, 158919, DOI: **10.1016/J.APSUSC.2023.158919**.

24 K. Ahmad, C. R. Chang and J. Li, Theoretical studies on copper-catalyzed arylation of nitrogen heterocycles from benzenediazonium acetate under ligand-free conditions, *J. Organomet. Chem.*, 2018, **864**, 50–57, DOI: **10.1016/J.JORGANCHEM.2018.01.006**.

25 M. Khalil, *et al.*, Suppressing the competing hydrogen evolution reaction in CO2 electroreduction: A review, *Renewable Sustainable Energy Rev.*, 2024, **206**, 114869, DOI: **10.1016/J.RSER.2024.114869**.

26 Y. Shang, L. Guo, Y. Shang and L. Guo, Facet-Controlled Synthetic Strategy of Cu2O-Based Crystals for Catalysis and Sensing, *Advanced Science*, 2015, **2**(10), 1500140, DOI: **10.1002/ADVS.201500140**.

27 M. Philip, A. R. Woldu, M. B. Akbar, H. Louis and H. Cong, A facile synthesis of Cu catalysts with multiple high-index facets for the suppression of competing H2 evolution during electrocatalytic CO2 reduction, *Nanoscale*, 2021, **13**(5), 3042–3048, DOI: **10.1039/D0NR07286A**.

28 D. Zhong, D. Cheng, Q. Fang, Y. Liu, J. Li and Q. Zhao, Understanding the restructuring and degradation of oxide-derived copper during electrochemical CO2 reduction, *Chem. Eng. J.*, 2023, **470**, 143907, DOI: **10.1016/J.CEJ.2023.143907**.

29 R. Elakkiya and G. Maduraiveeran, Hierarchical three-dimensional copper selenide nanocube microelectrodes for improved carbon dioxide reduction reactions, *Sustainable Energy Fuels*, 2021, **5**(24), 6430–6440, DOI: **10.1039/D1SE01458G**.

30 J. Yu, *et al.*, Enhancing the electrochemical reduction of carbon dioxide to multi-carbon products on copper nanosheet arrays *via* cation-catalyst interaction, *Cell Rep. Phys. Sci.*, 2023, **4**(4), 101366, DOI: **10.1016/J.XCRP.2023.101366**.

31 S. Choudhary, *et al.*, Oxidation mechanism of thin Cu films: A gateway towards the formation of single oxide phase, *AIP Adv.*, 2018, **8**(5), 55114, DOI: **10.1063/1.5028407/923119**.

32 H. Yan, Y. Sun, L. He and J. C. Nie, Transition metal oxide nanowires synthesized by heating metal substrates, *Mater. Res. Bull.*, 2011, **46**(11), 2120–2124, DOI: **10.1016/J.MATERRESBULL.2011.06.039**.

33 M. Košiček, J. Zavašnik, O. Baranov, B. Šetina Batič and U. Cvelbar, Understanding the Growth of Copper Oxide Nanowires and Layers by Thermal Oxidation over a Broad Temperature Range at Atmospheric Pressure, *Cryst. Growth Des.*, 2022, **22**(11), 6656–6666, DOI: **10.1021/ACS.CGD.2C00863**.

34 X. Jiang, T. Herricks and Y. Xia, CuO Nanowires Can Be Synthesized by Heating Copper Substrates in Air, *Nano Lett.*, 2002, **2**(12), 1333–1338, DOI: **10.1021/nl0257519**.

35 A. Shalav and R. G. Elliman, Volatile CuOH as a precursor for the growth of CuO nanowires, *Microelectron. Eng.*, 2013, **108**, 200–203, DOI: **10.1016/J.MEE.2013.01.033**.

36 R. Daiyan, *et al.*, 3D Heterostructured Copper Electrode for Conversion of Carbon Dioxide to Alcohols at Low Overpotentials, *Adv. Sustainable Syst.*, 2019, **3**(1), 1800064, DOI: **10.1002/ADSU.201800064**.

37 T. Sander, C. Reindl, M. Giar, B. Eifert, M. Heinemann, C. Heiliger and P. Klar, Correlation of intrinsic point defects and the Raman modes of cuprous oxide, *Phys. Rev. B:Condens. Matter Mater. Phys.*, 2014, **90**(4), 045203, DOI: **10.1103/PHYSREVB.90.045203**.

38 Y. Liu, F. Ren, S. Shen, Y. Fu, C. Chen, C. Liu, Z. Xing, D. Liu, X. Xiao, W. Wu, X. Zheng, Y. Liu and C. Jiang, Efficient enhancement of hydrogen production by Ag/Cu_2O/ZnO tandem triple-junction photoelectrochemical cell, *Appl. Phys. Lett.*, 2015, **106**(12), 123901, DOI: **10.1063/1.4916224**.

39 A. V Mazanik, A. I. Kulak, E. A. Bondarenko, O. V Korolik, N. S. Mahon and E. A. Streltsov, Strong room temperature exciton photoluminescence in electrochemically deposited Cu2O films, *J. Lumin.*, 2022, **251**, 119227, DOI: **10.1016/j.jlumin.2022.119227**.

40 C. Tan, *et al.*, Facet exposed-dependent surface bonding patterns between CuO and peroxymonosulfate vary activation mechanism: Reactive species and degradation pathways, *Results Eng.*, 2024, **23**, 102528, DOI: **10.1016/J.RINENG.2024.102528**.

41 N. Kumar, S. Limbu, S. Sharma and R. Narayan Chauhan, Impact of annealing on Cu2O doped with Na/Co: Structural, optical, and electrochemical consequences, *Inorg. Chem. Commun.*, 2024, **165**, 112538, DOI: **10.1016/J.INOCHE.2024.112538**.

42 Y. Dai, Q. Lin, Q. Wang, H. Zhao and Y. Li, Hierarchical CuO nanosheets encasing nanorods *via* a singular potential-cycling activation: Innovations in supercapacitor energy density and longevity, *J. Alloys Compd.*, 2024, **1008**, 176751, DOI: **10.1016/J.JALLCOM.2024.176751**.

43 A. Salova, S. F. Mahmud, N. K. A. Almasoudie, N. Mohammed, A. A. Albeer and R. F. Amer, CuO-Cu2O nanostructures as a sensitive sensing platform for electrochemical sensing of dopamine, serotonin, acetaminophen, and caffeine substances, *Inorg. Chem. Commun.*, 2024, **161**, 112065, DOI: **10.1016/J.INOCHE.2024.112065**.

44 P. Ulanski and C. Sonntag, Stability Constants and Decay of Aqua-Copper (III)–A Study by Pulse Radiolysis with Conductometric and Optical Detection, *Eur. J. Inorg. Chem.*, 2000, 2000, **6**, 1211–1217, DOI: **10.1002/(sici)1099-0682(200006)2000:6<1211::aid-ejic1211>3.3.co;2-t**.

45 H. Cohen, R. van Eldik, M. Masarwa and D. Meyerstein, Mechanism of oxidation of aquated copper(II) ions by hydroxyl free radicals. A high-pressure pulse-radiolysis experiment, *Inorg. Chim. Acta*, 1990, **177**(1), 31–34, DOI: **10.1016/S0020-1693(00)91905-4**.

46 Y. Zhao, *et al.*, Speciation of Cu Surfaces during the Electrochemical CO Reduction Reaction, *J. Am. Chem. Soc.*, 2020, **142**(21), 9735–9743, DOI: **10.1021/JACS.0C02354**.

47 T. Abiraman, E. Ramanathan, G. Kavitha, R. Rengasamy and S. Balasubramanian, Synthesis of chitosan capped copper oxide nanoleaves using high intensity (30 kHz) ultrasound sonication and their application in antifouling coatings, *Ultrason. Sonochem.*, 2017, **34**, 781–791, DOI: 10.1016/J.ULTSONCH.2016.07.013.

48 Y. E. B. Vidhya, A. Pattamatta, A. Manivannan and N. J. Vasa, Influence of fluence, beam overlap and aging on the wettability of pulsed Nd3+:YAG nanosecond laser-textured Cu and Al sheets, *Appl. Surf. Sci.*, 2021, **548**, 149259, DOI: 10.1016/J.APSUSC.2021.149259.

49 Y. H. Choi, D. H. Kim and S. H. Hong, p-Type aliovalent Li(I) or Fe(III)-doped CuO hollow spheres self-organized by cationic complex ink printing: Structural and gas sensing characteristics, *Sens. Actuators, B*, 2017, **243**, 262–270, DOI: 10.1016/J.SNB.2016.11.151.

50 D. J. dos Santos, N. M. Ito, M. C. L. de Oliveira, L. B. Tavares, M. C. Salvadori and R. A. Antunes, Preparation and characterization of copper thin film obtained by metal plasma immersion ion implantation and deposition, *Thin Solid Films*, 2018, **649**, 136–141, DOI: 10.1016/J.TSF.2018.01.048.

51 M. Nagar, D. Starosvetsky, J. Vaes and Y. Ein-Eli, Potassium sorbate as an inhibitor in copper chemical mechanical planarization slurry. Part I. Elucidating slurry chemistry, *Electrochim. Acta*, 2010, **55**(10), 3560–3571, DOI: 10.1016/J.ELECTACTA.2009.12.088.

52 G. P. W. Suyantara, T. Hirajima, H. Miki, K. Sasaki, S. Kuroiwa and Y. Aoki, Effect of H2O2 and potassium amyl xanthate on separation of enargite and tennantite from chalcopyrite and bornite using flotation, *Miner. Eng.*, 2020, **152**, 106371, DOI: 10.1016/J.MINENG.2020.106371.

53 B. Wolfsjäger, *et al.*, Hydrogen loading and reduction of iron oxides on steel studied by XPS with an *in situ* cell, *Appl. Surf. Sci.*, 2025, **689**, 162241, DOI: 10.1016/J.APSUSC.2024.162241.

54 H. Nassar, *et al.*, Fluorine tin oxide-supported copper nanofilms as effective and selective de-nitration electrocatalysts, *J. Electroanal. Chem.*, 2022, **911**, 116249, DOI: 10.1016/J.JELECHEM.2022.116249.

55 Z. Zhang, *et al.*, Highly dispersed Cu-Cu2O-CeOx interfaces on reduced graphene oxide for CO2 electroreduction to C2+ products, *J. Colloid Interface Sci.*, 2024, **661**, 966–976, DOI: 10.1016/J.JCIS.2024.01.173.

56 M. C. Biesinger, Advanced analysis of copper X-ray photoelectron spectra, *Surf. Interface Anal.*, 2017, **49**(13), 1325–1334, DOI: 10.1002/SIA.6239.

57 S. D. Giri, S. M. Mahajani, A. K. Suresh and A. Sarkar, Electrochemical reduction of CO2 on activated copper: Influence of surface area, *Mater. Res. Bull.*, 2020, **123**, 110702, DOI: 10.1016/J.MATERRESBULL.2019.110702.

58 M. Jafarian, M. Arjomandi and G. J. Nathan, Thermodynamic potential of molten copper oxide for high temperature solar energy storage and oxygen production, *Appl. Energy*, 2017, **201**, 69–83, DOI: 10.1016/J.APENERGY.2017.05.049.

59 A. R. Akbashev, Electrocatalysis on oxide surfaces: Fundamental challenges and opportunities, *Curr. Opin. Electrochem.*, 2022, **35**, 101095, DOI: 10.1016/J.COELEC.2022.101095.

60 A. Ali, *et al.*, Femtosecond laser-enabled facile tuning of Cu selectivity towards long-chain products in CO2 electroreduction, *J. CO2 Util.*, 2024, **85**, 102880, DOI: 10.1016/J.JCOU.2024.102880.

61 A. Ali and A. S. Alnaser, Laser-based fabrication of superhydrophobic carbide surfaces from waste plastics, *Surf. Interfaces*, 2024, **44**, 103602, DOI: 10.1016/j.surfin.2023.103602.

62 A. Ali, P. Piatkowski and A. S. Alnaser, Study on the Origin and Evolution of Femtosecond Laser-Induced Surface Structures: LIPSS, Quasi-Periodic Grooves, and Aperiodic Micro-Ridges, *Materials*, 2023, **16**(6), 2184, DOI: 10.3390/MA16062184.

63 P. Piatkowski, A. Ali, H. Alawadhi and A. S. Alnaser, Simultaneous Carburization, Oxidation, and Nitridation of Titanium Surface Using Ablation by Femtosecond Laser in n-Heptane, *Adv. Eng. Mater.*, 2023, **25**(6), 2201361, DOI: 10.1002/ADEM.202201361.

64 A. Ali, P. A. Piatkowski, H. Alawadhi and A. S. Alnaser, Reducing the Cut-In Voltage of a Silicon Carbide/p-Silicon Heterojunction Diode Using Femtosecond Laser Ablation, *ACS Appl. Electron. Mater.*, 2022, **4**(12), 6076–6086, DOI: 10.1021/ACSAELM.2C01204.

65 A. A. Baker, G. Boltaev, A. Ali and A. S. Alnaser, High sensitivity low-temperature ethanol and acetone gas sensors based on silver/titanium oxide decorated laser-induced graphene, *J. Mater. Sci.*, 2024, **59**(10), 4198–4208, DOI: 10.1007/S10853-024-09503-W/FIGURES/7.

66 A. Ali, *et al.*, A Two-Step Femtosecond Laser-Based Deposition of Robust Corrosion-Resistant Molybdenum Oxide Coating, *Materials*, 2023, **16**(3), 909, DOI: 10.3390/MA16030909.

67 S. Ahmad, M. Egilmez, A. M. Kannan and A. S. Alnaser, Oxygen evolution reaction enhancement of copper electrodes in alkaline medium using ultrafast femtosecond laser structuring, *Int. J. Hydrogen Energy*, 2024, **52**, 2–13, DOI: 10.1016/J.IJHYDENE.2022.10.239.

68 W. Ye, *et al.*, A Strongly Coupled Metal/Hydroxide Heterostructure Cascades Carbon Dioxide and Nitrate Reduction Reactions toward Efficient Urea Electrosynthesis, *Angew. Chem., Int. Ed.*, 2024, **63**(48), e202410105, DOI: 10.1002/ANIE.202410105.

69 J. J. Velasco-Vélez, *et al.*, The Role of the Copper Oxidation State in the Electrocatalytic Reduction of CO 2 into Valuable Hydrocarbons, *ACS Sustain. Chem. Eng.*, 2019, **7**(1), 1485–1492, DOI: 10.1021/ACSSUSCHEMENG.8B05106.

70 Z. Wang, *et al.*, Stabilizing the oxidation state of catalysts for effective electrochemical carbon dioxide conversion, *Chem. Soc. Rev.*, 2024, **53**(12), 6295–6321, DOI: 10.1039/D3CS00887H.

71 C. A. Obasanjo, *et al.*, In situ regeneration of copper catalysts for long-term electrochemical CO2 reduction to multiple carbon products, *J. Mater. Chem. A*, 2022, **10**(37), 20059–20070, DOI: 10.1039/D2TA02709G.